Materials Advances

ROYAL SOCIETY OF CHEMISTRY

PAPER

View Article Online
View Journal | View Issue

Cite this: *Mater. Adv.*, 2024, 5, 6630

The effect of mesoporous bioactive glass nanoparticles incorporating various metallic ions (Cu, Zn, Mn, Te) on wound healing

Sara Pourshahrestani,[a]* Ehsan Zeimaran,[a] Christina Janko,[b] Christoph Alexiou,[b] Andrea Kerpes,[b] Adrian Würz,[c] Marcus Fischer,[c] Hana Kaňková,[d] Martin Hartmann[c] and Aldo R. Boccaccini[a]*

Recently, mesoporous bioactive glasses (MBGs) as microparticles or nanoparticles (MBGNs) aroused a great interest owing to their high textural properties and capability to be incorporated with biologically active ions desirable for different stages of wound healing. Considering therapeutic effects of two well-recognized elements (copper and zinc) as well as two less-common elements (manganese and tellurium), in this study, different concentrations of these elements were incorporated into SiO_2–CaO MBGNs and their potential for wound healing applications was assessed *in vitro*. While at a concentration of 5 mg ml^{-1}, the extracts of some MBGNs reduced *E. coli* and *S. aureus* bacteria viabilities, normal human dermal fibroblast (NHDF) cell viabilities were negatively affected with extracts of Cu-MBGNs and Te-MBGNs. The nanoparticles also affected hemolysis in a donor-dependent manner and the incorporation of Te into the MBGNs networks increased the hemolysis ratio to more than 5%. Moreover, some of the nanoparticles at concentration of 1 mg ml^{-1} shortened activated partial thromboplastin time (aPTT) insignificantly compared to pure platelet poor plasma. At higher concentrations of therapeutic elements, the extracts of nanoparticles resulted in the significant slower migration of NHDF cells in the scratch area. The effects of the nanoparticles and their extracts on blood coagulation and NHDF cell migration are thus dependent on the composition and/or applied concentration of nanoparticles. The present results provide information for the design of MBGN compositions of interest for wound healing and highlight the importance of optimization of the nanoparticles dosage and therapeutic ion concentration for acceleration of the wound healing process.

Received 15th April 2024,
Accepted 22nd July 2024

DOI: 10.1039/d4ma00392f

rsc.li/materials-advances

1. Introduction

Traumatic injuries leading to uncontrolled bleeding and delayed wound healing represent serious health complications that may result in thousands of deaths annually.[1–3] In comparison to acute wounds which heal normally *via* four overlapping phases of hemostasis, inflammation, proliferation and remodeling, in chronic wounds, the wound healing process is affected and interrupted by some inevitable complications. For instance, it is reported that production of inflammatory mediators can be induced during wound infection, thereby entering the wound into a persistent inflammatory phase and impairing the wound healing process.[4–6]

Therefore, to overcome these clinical hurdles, various types of nanofibers, hydrogels, sponges, and particles composed of bioactive glasses, synthetic and/or natural polymers, proteins, and so on, have been proposed and their potentials to promote various stages of wound healing have been evaluated.[7–10] During the last decades, various compositions of porous and nonporous bioactive glasses in particulate form or as bioactive fillers in composite scaffolds and injectable hydrogels have gained increasing attention and the potential of these inorganic materials for wound healing applications is a subject of continuous research efforts.[6,11–14]

Mesoporous bioactive glasses (MBGs) in the SiO_2–CaO–P_2O_5 system were first synthesized in 2004 by Yan *et al.* *via* combination of supramolecular and sol–gel chemistry.[15] Mesoporous bioactive glasses nanoparticles (MBGNs), as member of the

[a] *Institute of Biomaterials, Department of Materials Science and Engineering, University of Erlangen-Nuremberg, 91058 Erlangen, Germany. E-mail: aldo.boccaccini@fau.de, sara.pourshahrestani@gmail.com*
[b] *Department of Otorhinolaryngology, Head and Neck Surgery, Section of Experimental Oncology and Nanomedicine (SEON), Else Kröner-Fresenius-Stiftung Professorship, University Hospital Erlangen, Erlangen, Germany*
[c] *Erlangen Center for Interface Research and Catalysis (ECRC), 91058 Erlangen, Germany*
[d] *FunGlass, Centre for Functional and Surface Functionalized Glass, Alexander Dubček University of Trenčín, Študentská 2, 911 50 Trenčín, Slovakia*

MBG family exhibiting much smaller particle size,[16] are of high interest for wound healing applications. These porous materials with excellent textural properties not only demonstrate unique biological characteristics such as good bioactivity and cytocompatibility but also have the capability to release therapeutic ions that can accelerate the different stages of wound healing, thanks to their outstanding exposed surface area, tunable pore size and volume.[17–22]

For instance, silicon (Si) as the major ionic component of silicate MBGs, has been found to stimulate collagen production and neovascularization;[12] calcium (Ca) plays an important role in hemostasis, the first stage of wound healing. Ca^{2+} ions are reported to be involved in the activation of the coagulation cascade[23] and promote thrombin generation, which contributes to the formation of a stable fibrin clot. Ca^{2+} ions are additionally found to modulate keratinocyte proliferation and differentiation, increase fibroblast proliferation and collagen synthesis.[12,24] To further enhance the biological functions of MBGs or MBGNs, more recently diverse therapeutic ions including silver (Ag),[17] gallium (Ga),[18] tantalum (Ta),[19] cerium (Ce),[25] strontium (Sr),[20] copper (Cu),[22,26,27] zinc (Zn),[3,27,28] boron (B)[29] and bismuth (Bi)[21] have been also incorporated into MBGs or MBGNs. The release of such biologically active ions was found to enhance various stages of wound healing, but also could impart other biological functions such as antibacterial activity. Zn and Cu, in particular, are antibacterial elements and Zn or Cu-containing MBGs or MBGNs alone or in combination with other biomaterials have been developed and evaluated for wound healing applications.[22,26–28,30]

Remarkably, the release of therapeutic dosages of Cu^{2+} ions from bioactive glasses has been extensively shown to exert antibacterial effect, stimulate angiogenesis, and induce vascular endothelial growth factor (VEGF) production, therefore accelerating the wound healing process.[26,31,32] For instance, in a study by Bari *et al.*, concentrations of 2 and 5 mol% of CuO were incorporated in MBGNs with a binary SiO_2–CaO composition and the results showed that Cu-MBGNs and their ionic dissolution products had antibacterial activities against *S. aureus*, *E. coli*, and *S. epidermidis* and were efficient in preventing and inhibiting biofilm formation by *S. epidermidis*.[33] MBGNs incorporated with 2 mol% CuO were also reported by Paterson *et al.*, and their potential for wound healing application was assessed. The results of this study demonstrated that the nanoparticles not only were biocompatible towards a monolayer of human primary fibroblast and a 3D human tissue engineered skin construct, but were also able to exert antibacterial effects against planktonic bacteria and disrupt biofilm formation in a 3D infected skin model.[22] The proangiogenic effects of the nanoparticles were also confirmed in this study. In another investigation by Romero-Sánchez *et al.*, the ionic products of MBGs and Cu-MBGs containing 5 mol% Cu were shown to stimulate angiogenesis when they were tested in an *in vivo* zebrafish embryo assay.[26]

Zn is another therapeutic element acquiring increasing attention in wound healing applications. It has been reported that Zn^{2+} ions can enhance platelet activation and aggregation, and promote fibroblast production and proliferation.[34,35] Notably, the ions are also well known to impart biomaterials with anti-inflammatory and antibacterial activities. For example, Zhu *et al.* fabricated an injectable hydrogel as a skin wound dressing *via* incorporation of Zn-MBGNs into alginate/chitosan composite.[3] It was found that the resultant hydrogel not only had antibacterial properties due to the synergistic effect of Zn-MBGNs and chitosan but also exhibited anti-inflammatory activity. The effect of the hydrogel on wound healing and angiogenesis was additionally improved after addition of Zn-MBGNs into the hydrogel. The results of this study showed that the secretion of angiogenic factors was stimulated by the presence of Zn-MBGNs.[3] Zn-MBGs were also incorporated into microporous starch and the resultant composites were found to have efficient antibacterial effect against *E. coli*. The *in vitro* and *in vivo* evaluations also showed that increasing the MBG content up to 15 wt% improved the capability of the composites to accelerate hemostasis and control bleeding.[28]

Tellurium (Te) is a poorly investigated element in wound healing applications. This element exhibits different oxidation states and its compounds have been found to have antitumoral, anti-inflammatory, antioxidant, and antibacterial properties.[36–38] Very recently, the potential of Te-containing bioactive glasses has started to be assessed for biomedical applications. For example, in a recent study by Miola *et al.*, a series of bioactive glasses doped with 1–5 mol% TeO_2 was developed *via* melt and quenching process and the resultant bioactive glasses were found to have bioactivity, anti-inflammatory ability, antibacterial effect against *S. epidermidis* and *S. aureus* and no toxicity towards hBMSCs.[39] Te-doped MBGNs with 1–5 mol% TeO_2 were also fabricated and investigated by Zhang *et al.*, for bone cancer therapy.[40] In addition to significant antibacterial effect against *E. coli* and *S. aureus*, the results of this study revealed that the presence of Te could induce cancer cell apoptosis to avoid bone cancer. Te nanoneedles (NNs) were also synthesized by Huang *et al.*, and it was shown that the fabricated Te NNs had excellent antibacterial activity against *S. aureus* and *E. coli via* puncturing bacterial membranes as well as promoting reactive oxygen species (ROS) generation in bacteria, therefore damaging the bacteria membrane.[41] In this study, Te NNs/PVA hydrogel was also prepared and its wound healing effect was evaluated in infected wound models. Faster healing of skin defects was observed in the presence of Te NNs/PVA hydrogel as compared to the PVA hydrogel and control-treated groups, suggesting the wound healing efficacy of Te NNs.[41]

Another less investigated element, manganese (Mn), has been reported to play important role in the maintenance of healthy bones and its deficiency can result in skeletal abnormalities.[36] It is been also noted that in the inflammatory stage of wound healing, inflammation-related cells can be regulated by some elements such as Mn and Zn, leading to the initiation and ending of an inflammatory response within an appropriate time frame.[35] Mn-containing MBGNs were prepared by Westhauser *et al.*, and it was demonstrated that the nanoparticles at low concentration did not exhibit toxicity and could induce pro-osteogenic features.[42]

Mn-doped calcium silicate (CS) nanowires were also incorporated into sodium alginate hydrogel and it was proven that Mn doping endows the CS nanowires with a photothermal effect so that the resultant hydrogel was able to kill tumor cells.[43] The release of Si^{4+} and Mn^{2+} ions from the hydrogel was also shown to synergistically promote wound healing when it was assessed using *in vitro* scratch assay and *in vivo* chronic skin wound models.[43]

Considering the favourable characteristics of Te and Mn mentioned above, however, to the best of our knowledge, there is no study evaluating the wound healing potential of Mn and Te when they are incorporated into MBGN frameworks. In the present study, our aim is therefore to develop SiO_2–CaO MBGNs containing various concentrations (1, 2 and 4 mol%) of Mn and Te as well as MBGNs containing two well-known elements (Zn and Cu) and to investigate the effects of such ion releasing MBGNs on the wound healing process using a series of *in vitro* studies.

2. Materials and methods

2.1. Materials

Hexadecyltrimethylammonium bromide (CTAB, Sigma-Aldrich), ethyl acetate (Sigma-Aldrich), ammonia solution (28–30% Sigma-Aldrich), tetraethyl orthosilicate (TEOS, Sigma-Aldrich), calcium nitrate tetrahydrate ($Ca(NO_3)_2{\cdot}4H_2O$, VWR), copper chloride, ($CuCl_2$, Sigma-Aldrich), zinc nitrate hexahydrate ($Zn(NO_3)_2{\cdot}6H_2O$, Sigma-Aldrich), sodium tellurite (Na_2TeO_3, Sigma-Aldrich) and manganese chloride tetrahydrate ($MnCl_2{\cdot}4H_2O$) (Merck, Germany) were used as received.

2.2. Synthesis of mesoporous bioactive glass nanoparticles containing Cu, Zn, Te and Mn

A microemulsion-assisted sol–gel method was utilized to fabricate Cu-MBGNs, Zn-MBGNs, Te-MBGNs, and Mn-MBGNs with 1, 2 and 4 mol % of Cu, Zn, Te and Mn which were substituted for Si or Ca (theoretical composition of MBGNs: $70SiO_2$–30CaO, Table 1).[44,45] Briefly, 2.8 g of CTAB was entirely dissolved by stirring in 132 ml of deionized water at 35 °C followed by addition of 40 ml ethyl acetate (allowed to stir for 30 min) and 28 ml of ammonia solution (1 M, allowed to stir for 15 min).

Table 1 Theoretical compositions of MBGNs incorporating Cu, Zn, Te and Mn

No.	Sample name	CuO, ZnO, MnO, TeO_2 (mol%)
1	MBGNs	—
2	1Cu-MBGNs	1 mol% CuO
3	2Cu-MBGNs	2 mol% CuO
4	4Cu-MBGNs	4 mol% CuO
5	1Zn-MBGNs	1 mol% ZnO
6	2Zn-MBGNs	2 mol% ZnO
7	4Zn-MBGNs	4 mol% ZnO
8	1Te-MBGNs	1 mol% TeO_2
9	2Te-MBGNs	2 mol% TeO_2
10	4Te-MBGNs	4 mol% TeO_2
11	1Mn-MBGNs	1 mol% MnO
12	2Mn-MBGNs	2 mol% MnO
13	4Mn-MBGNs	4 mol% MnO

Depending on the required composition, the proper amounts of TEOS, $Ca(NO_3)_2{\cdot}4H_2O$, $CuCl_2$, $Zn(NO_3)_2{\cdot}6H_2O$, Na_2TeO_3 or $MnCl_2{\cdot}4H_2O$ were then added into the prepared solution as described above stepwise in 30 min intervals. The solution was then left to stir for 4 h. Afterwards, precipitates were separated by centrifugation, and washed with deionized water and ethanol. Subsequently, the collected precipitates were dried at 60 °C overnight and calcined at 700 °C for 3 h in an electric furnace (heating rate of 1 °C min^{-1}).

2.3. Materials characterization

A field emission scanning electron microscope (FESEM) (Auriga, Zeiss, Germany) was utilized to analyze the microstructure and morphology of the synthesized nanoparticles. For FESEM analysis, the nanoparticles were sputtered coated with gold. The ImageJ software (National Institutes of Health, USA) was also used to determine the average particle size; 100 particles were chosen for each sample. To confirm the presence of the doping elements in MBGNs, energy-dispersive X-ray spectroscopy (EDS, Oxford Instruments, UK) was utilized. The textural properties of the fabricated MBGNs, Cu-MBGNs, Zn-MBGNs, Te-MBGNs, and Mn-MBGNs, were determined using nitrogen sorption measurements at 77 K, conducted on a Micromeritics porosimeter (ASAP 2010, Micromeritics GmbH). To evaluate the surface charge, the ζ potential of the undoped and doped MBGNs was measured by a Zetasizer Nano ZS (Malvern Instruments, UK). The chemical structure of the nanoparticles was assessed using attenuated total reflectance Fourier-transform infrared spectroscopy (ATR-FTIR, RAnity-1S, Shimadzu, Japan) in the region of 400–4000 cm^{-1} (wavenumber) and at a resolution of 4 cm^{-1}. An X-ray diffractometer (MiniFlex 600, Rigaku) in a 2θ range of 10°–60° (step size and speed of 0.02° and 1° min^{-1}, respectively) was utilized to investigate the amorphous nature or crystallinity of the synthesized nanoparticles.

2.4. Ion release studies

The ion release test was conducted in Dulbecco's modified Eagles's medium (DMEM) and Luria Bertani broth (LB) medium to investigate the time dependent concentrations of therapeutic ions released from the nanoparticles. Briefly, 10 mg of MBGNs were immersed in 10 ml DMEM and LB medium and incubated at 37 °C for up to 7 days, in case of DMEM, and for 1 day in case of LB medium. With respect to the ion release studies in DMEM, at specified time points, the samples were centrifuged and 5 ml of supernatants were collected and refilled with fresh DMEM. Notably, to stabilize the collected supernatants, concentrated nitric acid was added for both experiments in DMEM and LB medium and the samples kept them in the fridge until further analysis. The cumulative concentrations of ionic Si, Ca, Cu, Zn, Te and Mn released into DMEM were investigated using inductively coupled plasma optical emission spectroscopy (ICP OES SVDV 5100 (Agilent)). The existing concentrations of elements in DMEM and LB medium were subtracted from the measured values. For the preparation of calibration curves, calibration solutions were prepared by dilution of certified single-element reference

solutions (Analytika, s.r.o. Praha). Independent calibration verification was performed using multi-element solutions (Merck). To deal with non-spectral interference, the method of continuous measurement of the internal standard in axial and radial view was used (scandium was chosen as the internal standard). The pH values of DMEM with the nanoparticles were also measured. The experiments were conducted in triplicate or four replicates for each sample.

2.5. Antibacterial assay

To assess the effect of ionic dissolution products from synthesized MBGNs, Cu-MBGNs, Zn-MBGNs, Te-MBGNs, and Mn-MBGNs on bacteria viability, an indirect antibacterial study was conducted using *E. coli* (Gram-negative, ATCC25922) and *S. aureus* (Gram-positive, ATCC25923). The *E. coli* and *S. aureus* bacteria were incubated in LB medium for 24 h at 37 °C. Afterwards, the optical density (OD) of both bacteria was adjusted at 0.015 (Thermo Scientific GENESYS 30, Germany) at 600 nm. Briefly, after sterilizing the nanoparticles at 160 °C for 2 h in a furnace (Naberthem, Germany), they were added in LB medium at concentrations of 5 mg ml^{-1}, followed by incubation for 24 h at 37 °C. To collect extract (particle free supernatant), LB media containing the particles were then filtered out using 0.22 μm pore size filters and were further diluted to 1 and 0.1 mg ml^{-1}. Afterwards, the extracts were added to 24 well-plates (1 ml of each extract) with 20 μl bacteria suspension and were incubated for 6 and 24 h at 37 °C. The bacterial cell suspension in LB medium and pure LB medium were used as control and blank, respectively. The experiment was carried out in triplicate for each sample. After each time point, the OD values were measured and relative bacterial viability was calculated as follows:

$$\text{Relative bacterial viability (\%)} = (OD_{sample} - OD_{blank}/OD_{control} - OD_{blank}) \times 100$$

The obtained OD value for the control was normalized as 100%.

2.6. *In vitro* biocompatibility

To detect the effects of dissolution products of the nanoparticles, indirect biocompatibility assay was conducted using Normal human dermal fibroblast (NHDF) cells (Promocell, Germany). The cells were received from Translation Research Center of Friedrich-Alexander University Erlangen-Nuremberg. The NHDF cells were cultured in high glucose DMEM (4.5 g L^{-1}) supplemented with 1% penicillin/streptomycin solution and 10% fetal bovine serum (FBS), followed by incubation at 37 °C in 5% CO_2. The NHDF cells were then seeded at a density of 50 000 cells per well into a 24-well plate and incubated at 37 °C for 24 h. The sterilized MBGNs, Cu-MBGNs, Zn-MBGNs, Te-MBGNs, and Mn-MBGNs were soaked in DMEM for 24 h at a concentration of 5 mg ml^{-1}. Next, to obtain the extracts (DMEM with dissolution products), suspensions (DMEM containing nanoparticles) were centrifuged and filtered out. The extracts were further diluted to concentrations of 1 and 0.1 mg ml^{-1}. Afterwards, the extracts were incubated with NHDF cells at 37 °C for further 48 h and then cell viability was assessed by WST-8 assay (CCK-8 Kit, Sigma-Aldrich). After incubation of the cells with 2% v/v WST-8 in DMEM for 3 h, 100 μl from each 24-well plate was transferred to a 96 well-plate to measure the absorbance (Ab.) at 450 nm using a microplate reader (PHOmo, Anthos Mikrosysteme GmbH, Germany). The following equation was utilized to calculate the cell viability (%):

$$(Ab._{sample} - Ab._{blank}/Ab._{control} - Ab._{blank}) \times 100$$

NHDF cells in DMEM and pure WST-8 solution were used as positive control (CNT) and blank, respectively. The experiment was performed in triplicate for each sample. The absorbance of CNT was normalized as 100%.

After determination of cell viabilities, the NHDF cells cultured with the extracts of the nanoparticles at concentration of 1 mg ml^{-1} were stained with calcein and DAPI and cell morphology was analyzed by fluorescence microscopy (Axio Scope A1, Carl-Zeiss, Germany). Briefly, after washing NHDF cells with DPBS, calcein staining solution (4 μl ml^{-1}) was added, followed by incubation at 37 °C for 45 min. The calcein solution was then removed and NHDF cells were washed with DPBS and Fluo-Fix solution (3.7% formaldehyde in DPBS) was added. After 15 min incubation at room temperature, the NHDF cells were washed with DPBS, and DAPI staining solution was added and left for 5 min. After removing the DAPI solution, DPBS was added and the stained NHDF cells were stored at 4 °C until further analysis.

2.7. Hemolysis assay

To investigate the hemocompatibility of nanoparticles, an hemolysis assay was performed. Human blood was obtained from healthy volunteers for hemolysis assay and plasma coagulation tests. The use of human material was approved by the ethics committee of the Friedrich-Alexander-Universität Erlangen-Nürnberg (# 21-383-2-B). 10 mg MBGNs were taken up in 10 ml PBS and 40 μl lithium heparin anticoagulated whole blood was added, resulting in 1 mg ml^{-1} MBGNs, which were incubated for 1 h at 37 °C while carefully shaking. 1% Triton X-100 in water served as positive control (PC), PBS served as negative control (NC). After 1 h, erythrocytes or red blood cells (RBCs) were sedimented by centrifugation at 800 × *g* for 15 min. 200 μl supernatant were transferred into 96 well plates and absorption at 541 nm was measured in duplicates on Spectramax iD3 Plattenphotometer (Molecular Devices). The hemolysis ratios of the RBCs were calculated using the following formula:

$$\text{Hemolysis ratio (\%)} = (OD_{sample} - OD_{NC}/OD_{PC} - OD_{NC}) \times 100.$$

2.8. Plasma coagulation

To characterize the effect of nanoparticles on the activation of blood coagulation cascade, activated partial thromboplastin time (aPPT) and prothrombin time (PT) were measured. To obtain platelet-poor plasma (PPP), sodium citrate anticoagulated blood was centrifuged at 2500 × *g* for 15 min.

Particles were incubated overnight at 60 °C to dry them. Then, 10 mg, 5 mg and 1 mg MBGNs were weighed into tubes and preincubated for 15 min at 37 °C in 100 µl PPP. Then, MBGNs were further diluted with PPP for the coagulation tests. Plasma samples with abnormal and normal coagulation times (DiaSys, Flacht, Germany) were used as positive and negative controls. Measurements were performed in triplicates. For analysis of the aPPT, 4 µl were diluted with 396 µl PPP and from that, 100 µl were added into prewarmed tubes. 100 µl aPPT solution (DiaSys, Flacht, Germany) was added before adding 100 µl 25 mM $CaCl_2$ solution. MC4 Plus coagulometer (Merlin Medical, Lemgo, Germany) was used to record the time until coagulation. For analysis of the PT, 600 µl MRX PT buffer (DiaSys, Flacht, Germany) was diluted with 100 µl PPP. From that, 20 µl were added to 180 µl PPP in prewarmed tubes. Then, the assay was started with 200 µ MRX PT Owren (DiaSys, Flacht, Germany) and the time until coagulation was recorded.

2.9. *In vitro* cell migration analysis (scratch assay)

The migration of NHDF cells in the presence of the extracts of MBGNs, Cu-MBGNs, Zn-MBGNs, Te-MBGNs and Mn-MBGNs at the concentration of 1 mg ml^{-1} was investigated according to a typical *in vitro* scratch assay. The NHDF cells were first seeded into 12-well plate at 100 000 cells per well and incubated at 37 °C for 24 h until a monolayer was formed. A scratch was then made in each well using a sterile micropipette tip (100 µL) and thereafter a NHDF monolayer was washed with DPBS to remove cell debris, followed by addition of the extracts at concentration of 1 mg ml^{-1}. The microscopic images were captured (Axio Scope A1, Carl-Zeiss, Germany) at different time points (0 h and 24 h) and analyzed by ImageJ. The following equation was used to calculate the percentage of wound closure over time:

$$\text{Wound closure percentage (\%)} = (A_0 - A_t/A_0) \times 100$$

where A_0 and A_t are the initial wound area at time zero and the wound area at the specified time, respectively. The NHDF cells treated with DMEM were considered as CNT. The experiment was carried out in triplicate for each sample.

2.10. Statistical analysis

The data are reported as mean ± standard deviation (SD) and one-way analysis of variance (ANOVA) with Tukey's *post hoc* analysis was used to analyze the statistical differences between groups. The significance level was considered as $p < 0.05$ and marked by (*).

3. Results and discussion

3.1. Morphological and structural characterization

The process of MBGNs formation is schematically illustrated in Fig. 1(a). In this procedure, CTAB micelles guide mesopore formation and oil-in-water microemulsion droplets that act as nanoparticle templates are formed after addition of EA.[29] MBGNs are obtained after washing and calcination at 700 °C. The morphologies of MBGNs doped with different concentrations of Cu, Zn, Mn, Te were observed by FESEM and the representative images (Fig. 1(b)) demonstrate that the MBGNs have mainly a sphere-like shape with visible pores and particle size ranging between 100 and 200 nm (Table 2), as measured by the ImageJ software. Our results are in good agreement with previously reported results in the literature where Cu-MBGNs, Zn-MBGNs, Te-MBGNs and Mn-MBGNs were reported to have sphere-like shape morphologies.[33,40,46,47] However, increasing the concentration of Te affected the morphology of 4Te-MBGNs so that a uniform spheroidal morphology was not observed for some particles.

To investigate the compositions of MBGNs containing Cu, Zn, Mn and Te, EDS analysis was conducted. Fig. 2 illustrates the EDS spectra of undoped and doped MBGNs (2 and 4 mol% of therapeutic ions). The results confirmed the successful incorporation of Cu, Zn, Te and Mn into SiO_2–CaO MBGNs. The relative atomic percentages of Si, Ca, Cu, Zn, Te and Mn are also shown in Fig. 2.

The textural properties of bioactive glasses including surface area and pore volume are important for their interaction with cells. For instance, bioactive glasses with high surface area and pore volume may be efficient in early stage of wound healing as they are able to absorb water from blood, therefore concentrating blood components and speeding up the hemostasis process.[11,18,48] As evident from the type IV nitrogen sorption isotherms with H3 hysteresis loops (Fig. 3(a)–(f)), all undoped and doped MBGNs are mesoporous with slit-shaped pores. Except 4TeMBGN, all the nanoparticles were found to have two main pore sizes, the smaller pores at ~3.3 nm and the larger pores at ~6.3 nm. While the MBGNs had the highest pore volume in the range of 6.3 nm, most of the nanoparticles have a higher pore volume in the range of 3.3 nm (Fig. 3(g)–(j)). The BET surface areas and total pore volumes of the nanoparticles are summarized in Table 2. All nanoparticles except 4Te-MBGNs exhibited BET surface areas in the range between 262 and 579 $m^2\ g^{-1}$ and total pore volumes between 0.29 and 0.61 $cm^3\ g^{-1}$. However, with increasing concentration of Cu, Zn, Te and Mn in the MBGN frameworks, the BET surface area and total pore volume of the MBGNs were reduced. However, all Cu-MBGNs, 1 and 2 Zn-MBGNs, 1 Te-MBGNs, and Mn-MBGNs still exhibit BET surface areas of more than 400 $m^2\ g^{-1}$. As shown in Table 2, the reduction of surface area was more pronounced with increasing concentration of Te.

The ζ potential values of the all MBGNs, Cu-MBGNs, Zn-MBGNs, Te-MBGNs and Mn-MBGNs, were measured and the results are shown in Table 2. All nanoparticles displayed negatively surface charge in deionized water, which can be ascribed to the presence of negatively charged silanol groups on the nanoparticles' surface. As the results demonstrated, the incorporation of therapeutic elements in MBGNs led to a decrease in the zeta potential values of the nanoparticles. As previously reported, negatively charged surfaces can activate intrinsic pathways of the coagulation cascade (early stage of wound healing). It is reported that this activation can occur *via* binding positively charged amino acids in clotting factor XII chain to the negatively-charged silanols surface.[49,50]

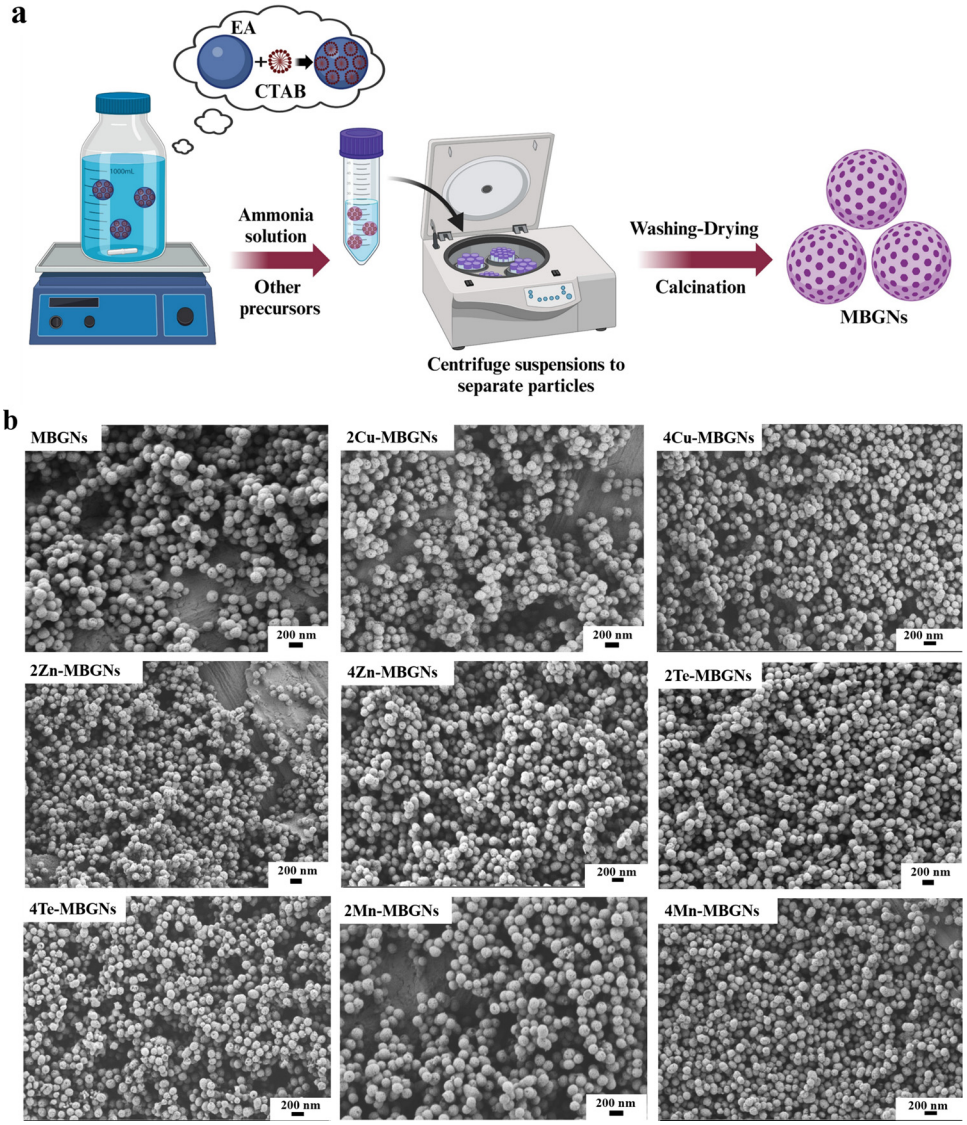

Fig. 1 (a) Schematic representation the formation of MBGNs (created with biorender.com), (b) representative FESEM micrographs showing the morphology of MBGNs, 2 and 4Cu-MBGNs, 2 and 4Zn-MBGNs, 2 and 4Te-MBGNs, 2 and 4Mn-MBGNs.

Table 2 Zeta potential, particle sizes and textural properties of MBGNs, Cu-MBGNs, Zn-MBGNs, Te-MBGNs and Mn-MBGNs

No.	Sample name	Zeta potential	Particle size (nm)	BET surface area ($m^2\ g^{-1}$)	Total pore volume ($cm^3\ g^{-1}$)
1	MBGNs	±−11.9 ± 0.3	±148 ± 13	554	0.619
2	1Cu-MBGNs	±−15.1 ± 0.6	±137 ± 13	519	0.445
3	2Cu-MBGNs	±−13.6 ± 0.3	±138 ± 12	486	0.444
4	4Cu-MBGNs	±−14.7 ± 0.5	±133 ± 11	477	0.404
5	1Zn-MBGNs	±−16.8 ± 0.2	±156 ± 16	579	0.497
6	2Zn-MBGNs	±−15.9 ± 0.2	±134 ± 12	462	0.420
7	4Zn-MBGNs	±−16.8 ± 0.6	±146 ± 12	370	0.376
8	1Te-MBGNs	±−12.1 ± 0.6	±151 ± 15	480	0.395
9	2Te-MBGNs	±−12.0 ± 0.1	±140 ± 15	262	0.294
10	4Te-MBGNs	±−14.2 ± 0.4	±132 ± 15	42	0.075
11	1Mn-MBGNs	±−12.0 ± 0.6	±160 ± 14	550	0.500
12	2Mn-MBGNs	±−13.8 ± 0.5	±139 ± 13	505	0.489
13	4Mn-MBGNs	±−16.2 ± 0.2	±134 ± 13	498	0.468

Similar to silicate glasses, FTIR spectra of all nanoparticles demonstrated bands located at ~440–450 cm^{-1}, ~792–802 cm^{-1}, ~1050–1200 cm^{-1}, which are attributed to Si–O–Si rocking, bending and stretching vibrations, respectively (Fig. 3(k),

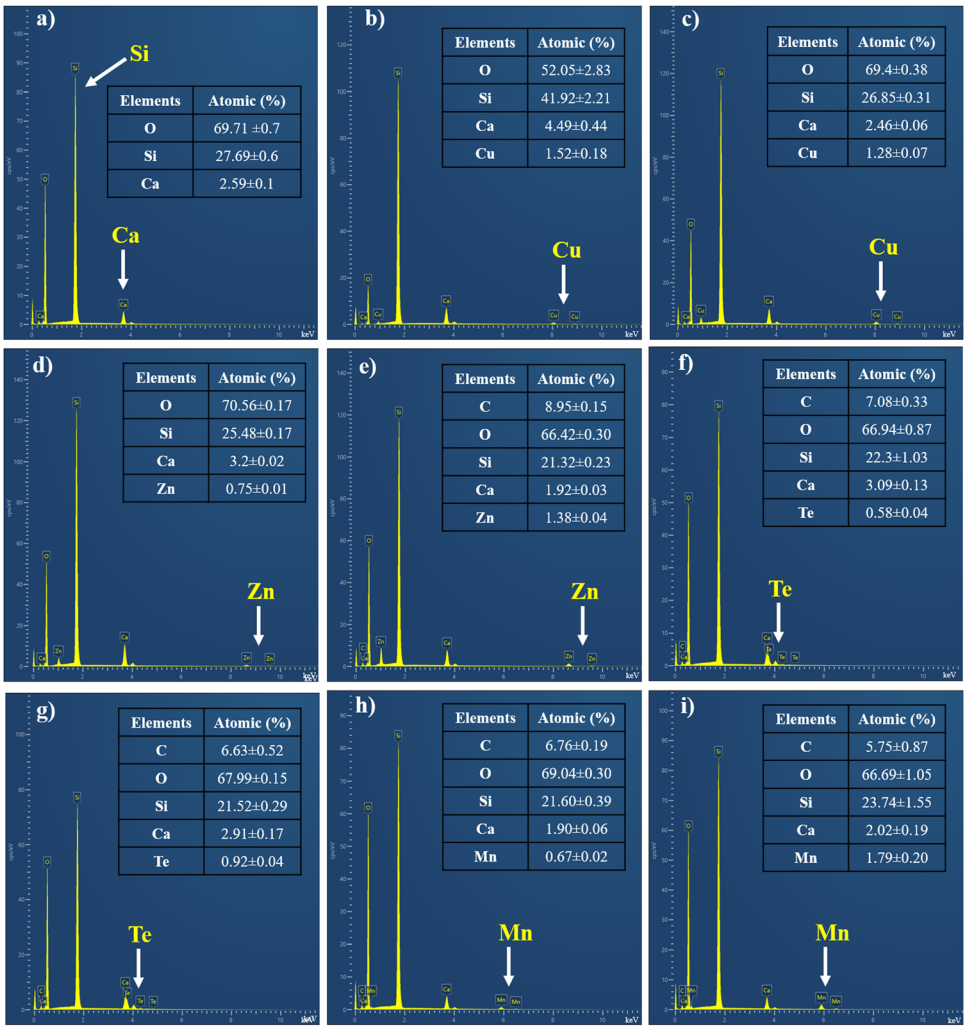

Fig. 2 The EDS spectra and atomic percentages of (a) MBGNs, (b) 2Cu-MBGNs, (c) 4Cu-MBGNs, (d) 2Zn-MBGNs, (e) 4Zn-MBGNs, (f) 2Te-MBGNs, (g) 4Te-MBGNs, (h) 2Mn-MBGNs, and (i) 4Mn-MBGNs.

highlighted in gray). The result confirmed the successful formation of the glass network. The FTIR spectrum of 4Te-MBGN also showed a peak at around 680 cm^{-1} which is ascribed to the Te–O vibration (indicated by black arrow).[39]

The XRD patterns of MBGNs, 2–4Cu-MBGNs, 2–4Zn-MBGNs, 2–4Te-MBGNs and 2–4Mn-MBGNs are demonstrated in Fig. 3(l). Except for the nanoparticles doped with higher concentrations of Cu and Te, all nanoparticles showed only a broad band at around 2θ (°) = ~23°, which demonstrates the amorphous nature of the fabricated nanoparticles. However, several diffraction peaks located at 2θ (°) = ~35.6°, 38.7°, and 48.7° were observed in 4Cu-MBGNs which corresponds to the crystallographic planes of CuO.[45] Other peaks additionally appeared in MBGNs with higher concentrations of Te, which may be assigned to tellurium oxide.[51]

3.2. Ion release measurements in DMEM and LB medium

The pH of DMEM after immersion of the nanoparticles for 1 and 7 days was measured and the results are depicted in Fig. 4. As can be seen from the results, the presence of nanoparticles altered the pH of DMEM during 7 days incubation so that the pH of DMEM, which was initially around 7.5, rose to around 7.9–8 after 7 days incubation. This notable increase of the DMEM pH value can be attributed to the MBGNs dissolution, resulting in rapid exchange of cations from the nanoparticles with H^+ from the medium.[52,53]

It is evidenced that biological responses including cell functions (proliferation and migration of epithelial, keratinocyte and fibroblast cells), angiogenesis, antibacterial and hemostatic efficiency can be induced by the released ionic dissolution products from bioactive glasses.[13,45,54] Therefore, to assess the release profiles of the nanoparticles in DMEM and LB medium, the ionic concentrations of Si, Ca, Cu, Zn, Te and Mn, released from MBGNs, were measured using ICP-OES for up to 7 d in DMEM and for 1 day in LB medium. The cumulative ion release profiles of undoped and doped MBGNs were assessed in DMEM and the results are shown in Fig. 4. A continuous release of Si ions was observed for all the nanoparticles, representing the well-known sustained dissolution of MBGNs in aqueous media. However, among the nanoparticles,

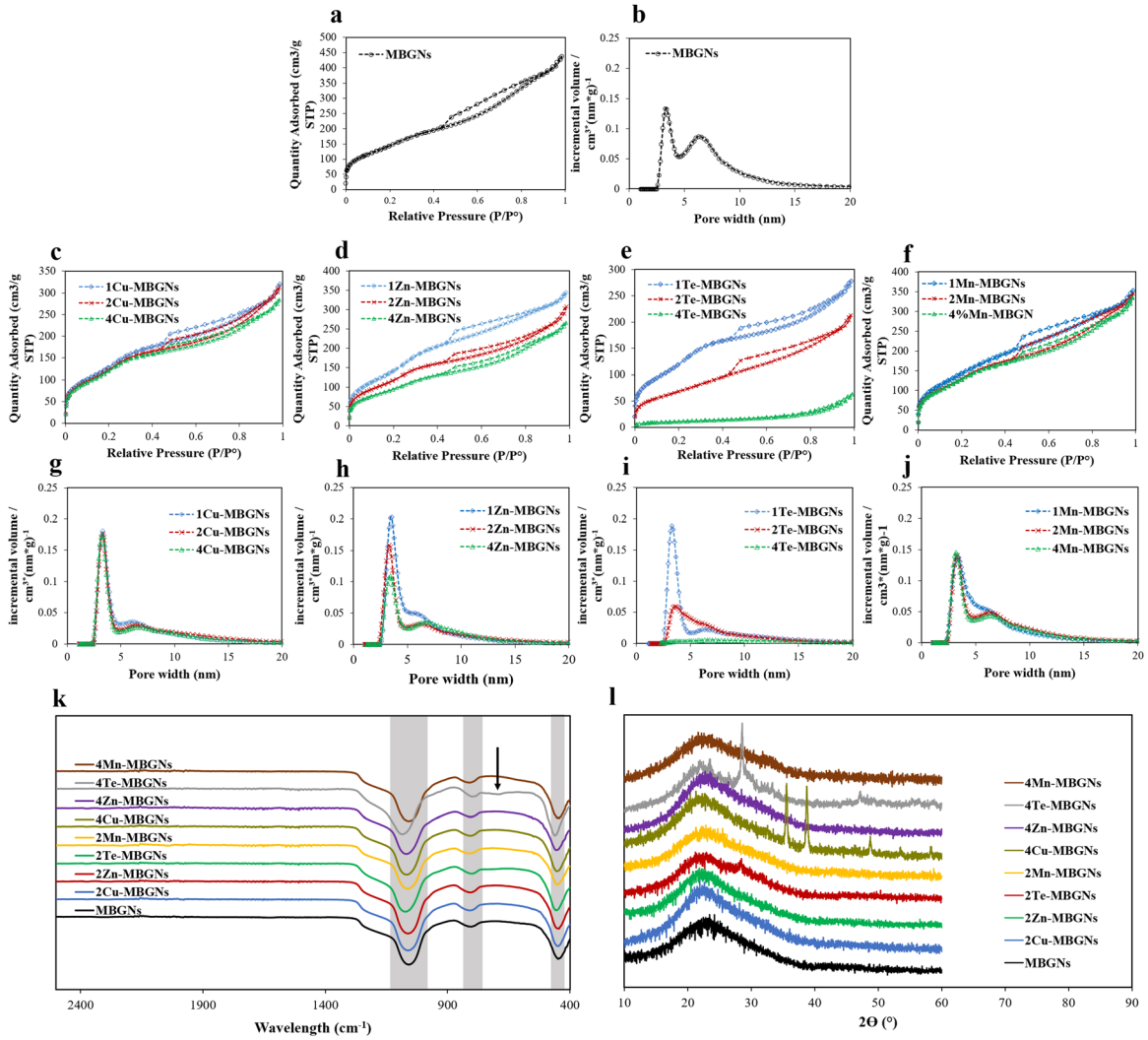

Fig. 3 (a)–(f) Nitrogen sorption isotherms of the nanoparticles, measured at 77 K and (g)–(j) pore size distributions, representative. (k) FTIR spectra and (l) XRD patterns of MBGNs with 2 and 4 mol% of Cu, Zn, Te and Mn.

4Te-MBGNs showed the lowest concentration of released Si ion (around 30 mg l^{-1}) after 7 days of immersion, which suggested that increasing Te content may negatively affect the dissolution of MBGNs. However, in a study by Zhang *et al.*, it was found that the degradation rate of MBGNs was not significantly affected by the incorporation of high amount of Te ions.[40] The authors discussed that silicon sites of the nanoparticle's framework were occupied by Te^{4+} ions. Notably, burst releases of Ca and other incorporating ions were observed for most the nanoparticles withing the first 24 h incubation. It may be assumed that these ions are mostly adsorbed onto the nanoparticle surface, allowing them to be released rapidly. It should be pointed out that to achieve the diffusion of ions into the nanoparticle's inner parts, a heat treatment is needed.[45] While Mn-MBGNs exhibited an increasing trend of Ca release at day 1 and 3 followed by a decreasing trend at day 7, the ion release profiles of the rest of the nanoparticles showed increasing trends with a continuous release over 7 days incubation, demonstrating the continuous dissolution of the undoped and doped MBGNs over time. While the 2Cu-MBGNs (around 11 mg l^{-1}) and 4Mn-MBGNs (around 13 mg l^{-1}) resulted in the lowest release of Ca ions, the highest release was measured for 2Te-MBGNs composition. With increasing Cu, Zn, Te and Mn contents, their released concentrations were also increased. Overall, it is important to point out that the fabricated nanoparticles are degradable due to the release of Si and other therapeutic ions,[47] which further stimulates desired biological functions.

To assess the ion release profiles of the nanoparticles in LB medium, the different MBGN samples were additionally incubated in LB medium for 1 day, followed by measuring the concentrations of Si, Ca, Cu, Zn, Te and Mn ions released in LB medium. The results in Fig. 5 show that 1Te-MBGNs and 4Te-MBGNs exhibited the highest (around 34 mg l^{-1}) and lowest (around 12 mg l^{-1}) release of Si ions, respectively. On the other hand, 1 and 2Te-MBGNs compositions presented the highest release of Ca ions, while the lowest concentration of Ca was observed for 2Cu-MBGNs (around 19 mg l^{-1}) and 4Mn-MBGNs (around 16 mg l^{-1}) compositions. These results

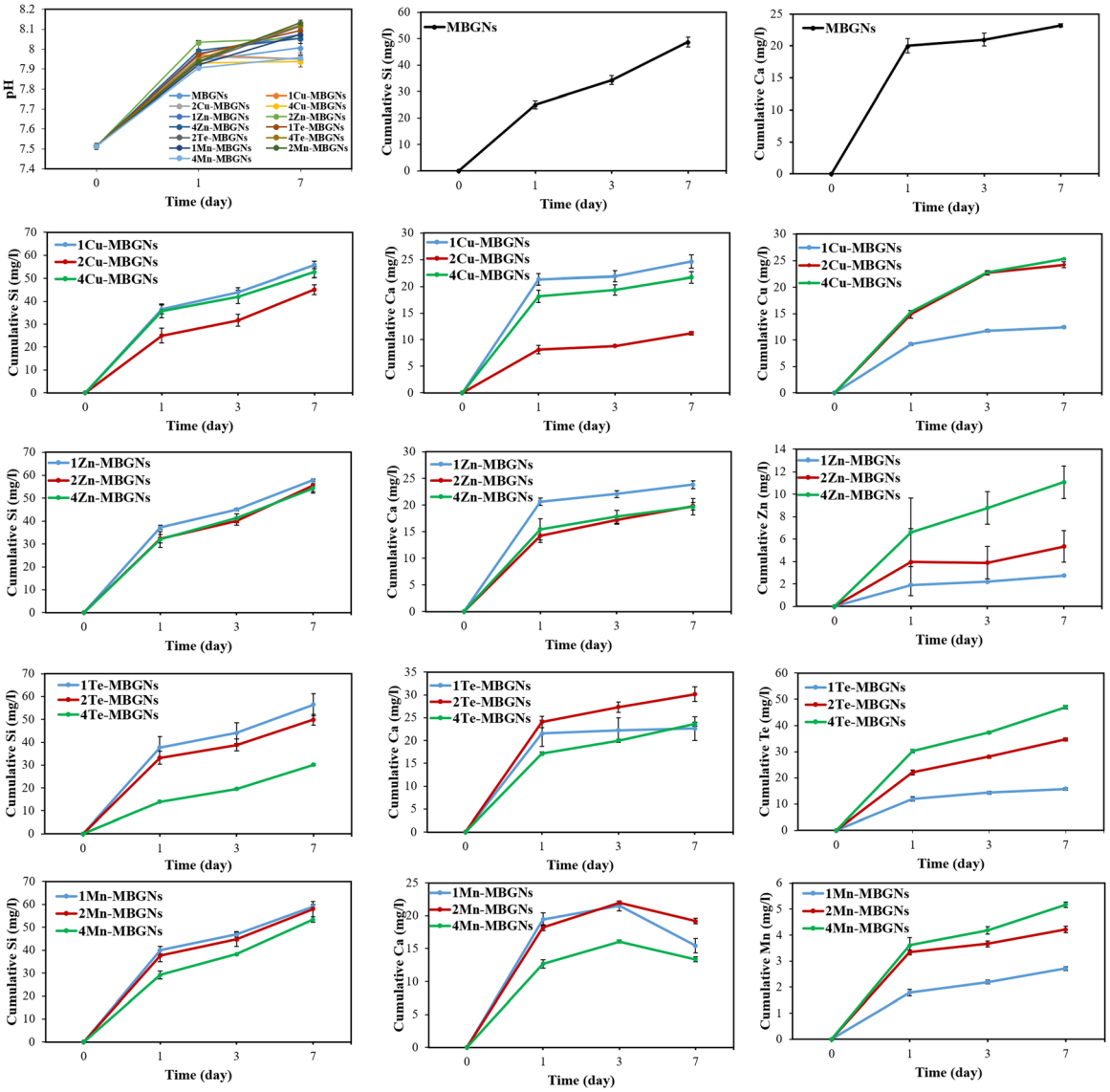

Fig. 4 pH measurement of the nanoparticles in DMEM after 1 and 7 days of incubation (upper left) and cumulative ion release profiles of doped and undoped MBGNs during immersion in DMEM for 1, 3 and 7 days, measured by ICP-OES.

correlate with the results of the ions release study in DMEM, where 4Te-MBGNs showed the lowest concentration of Si ions and the lowest Ca concentrations were recorded for 2Cu-MBGNs and 4Mn-MBGNs. The results further revealed that increasing the Cu, Zn, Te and Mn contents in SiO_2–CaO MBGNs led to an increase of the released concentrations in LB medium, which may induce antibacterial effects of the nanoparticles against both Gram-negative and positive bacteria.

3.3. Assessment of bacteria viability after incubation with extracts

One of the major complications facing surgical wounds or trauma is bacterial infections which can delay the wound healing process, thereby requiring that the utilized wound healing materials have antibacterial efficacy. Therefore, in this study, the effect of extracts of the nanoparticles in the concentrations of 0.1, 1 and 5 mg ml^{-1} on the viabilities of *E. coli* and *S. aureus* after culture for 6 and 24 h was evaluated. As the results demonstrated, the highest inhibitory effect on the viability of the bacteria was observed after 6 h incubation of the extracts with both Gram-negative and positive bacteria. For *E. coli*, while the bacteria viability was more than 90% after incubation with the extracts of MBGNs, Cu-MBGNs, Zn-MBGNs, and Mn-MBGNs in the concentration of 0.1 mg ml^{-1}, Te-MBGNs significantly reduced the *E. coli* viability to less than 15%, as compared to the control. In the concentration of 1 mg ml^{-1}, Te-MBGNs also led to the lowest bacteria viability in comparison to other nanoparticles where the *E. coli* viability was found to be less than 10%. At concentration of 5 mg ml^{-1}, the extracts of the Te-MBGNs additionally demonstrated the highest inhibitory effect on the bacteria viability in comparison to others. The 2 and 4Cu-MBGNs as well as Zn-MBGNs also

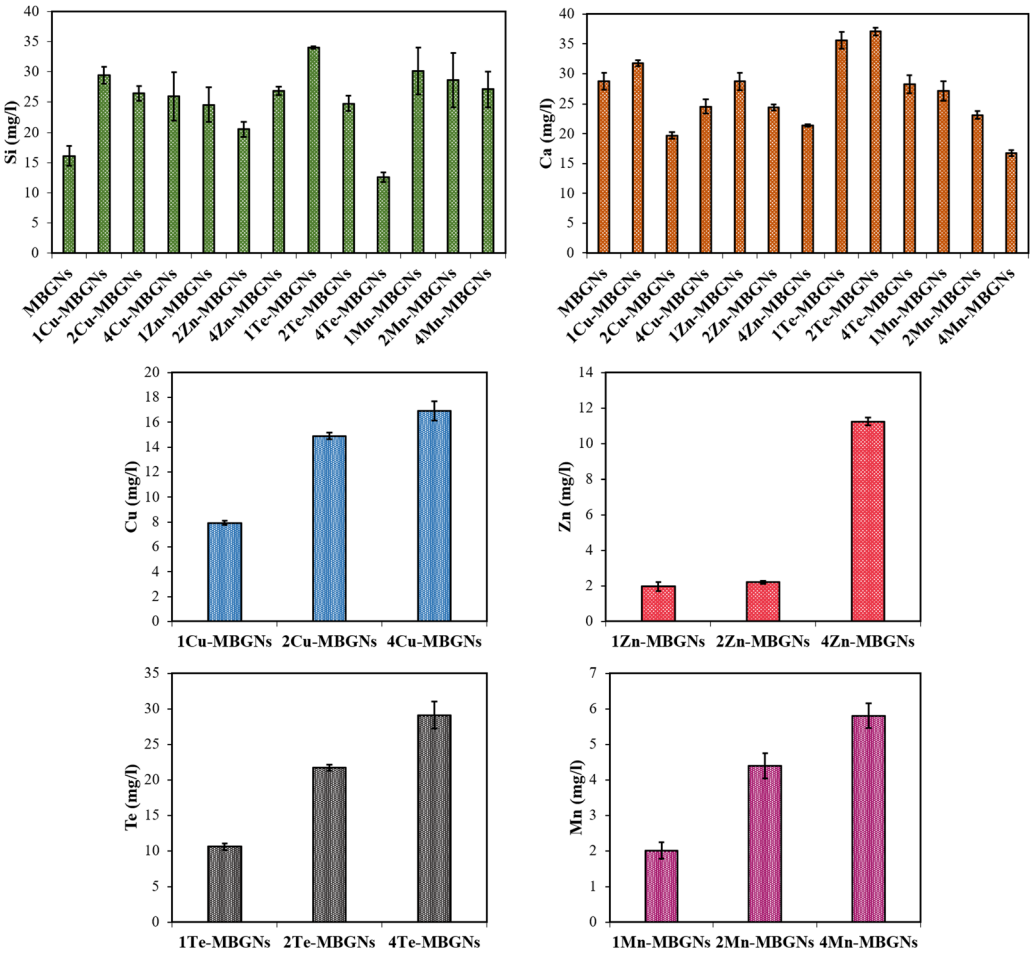

Fig. 5 Si, Ca, Cu, Zn, Te and Mn release profiles upon immersion of nanoparticles in LB medium.

significantly diminished bacterial viability in comparison to the control (Fig. 6). After 24 h incubation of the extracts with *E. coli*, the 2 and 4Te-MBGNs at concentration of 5 mg ml^{-1} resulted in the lowest bacteria viabilities (<20%) followed by 1Te-MBGNs, 4Cu-MBGNs and 4Zn-MBGNs which resulted in around <85% bacteria viabilities, being more effective against *E. coli* than MBGNs and Mn-MBGNs compositions.

Interestingly, the extracts of Te-MBGNs in concentration of 0.1, 1 and 5 mg ml^{-1} additionally displayed the highest inhibitory effect on *S. aureus* viability after 6 incubation (<40%) (Fig. 7). Furthermore, the bacteria viability was reduced to less than around 30% after incubation with the extracts of 2 and 4Cu-MBGNs and 4Zn-MBGNs in concentration of 5 mg ml^{-1}. At 24 h incubation, not only 2 and 4Te-MBGNs at concentrations of 1 and 5 mg ml^{-1} resulted in the lowest bacteria viabilities with respect to the control, the 4Cu-MBGNs in all concentrations as well as 2Cu-MBGNs and 4Zn-MBGNs in the concentration of 5 mg ml^{-1} reduced the cell viabilities significantly in comparison to the control. It should be noted that extracts of Te-MBGNs at some concentrations (5 mg ml^{-1} or 1 mg ml^{-1}) also led to a change of the colour of the medium (to black) after 24 h incubation for both experiments with *E. coli* and *S. aureus*.

Overall, the results presented here demonstrate that the antibacterial activity of the dissolution products of the nanoparticles strongly depend on the concentration of the doping ions and also on the utilized amount of nanoparticles to prepare extracts. Notably, the Te-MBGNs series was found to have the highest inhibitory effect on the viabilities of both negative and positive bacteria strains in comparison to the rest of the nanoparticles. The results of the ion release study in LB medium indicated that with increasing Te content, the concentration of released Te ions increased from around 10 mg l^{-1} to around 29 mg l^{-1}. The antibacterial effect of Te-MBGNs can thus be attributed to the presence of Te ions, as with increasing its content, the antibacterial properties of the compositions were improved.

Our results are in good agreement with the studies of Miola *et al.*[39] and Zhang *et al.*,[40] where Te-MBGNs compositions were reported to significantly reduce the number of viable bacteria. Notably, it has been reported by Miola *et al.*, that Te could bestow excellent antibacterial activity to bioactive glasses while preserving cell viability.[39] It was demonstrated that the bioactive glass containing 5% Te is able to reduce the number of *S. aureus* or *S. epidermidis* bacteria significantly while BMSCs viability was preserved when it was tested using a cells-bacteria

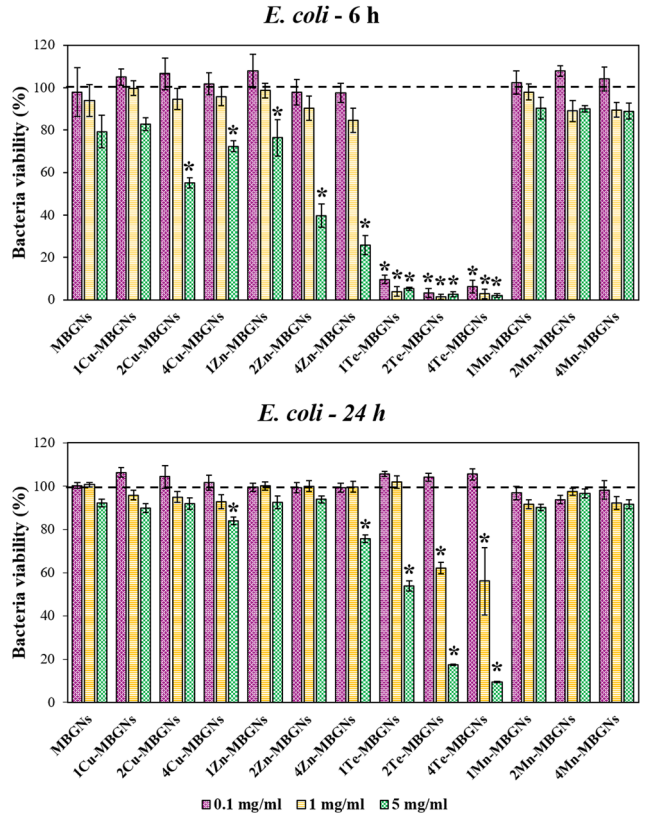

Fig. 6 *E. coli* viabilities after 6 and 24 h treatment with the extracts of different MBGNs investigated (samples in triplicate; mean values and SD from 4–6 measurements). The significance differences ($p < 0.05$, marked by (*)) are indicated as compared to the control (shown by the dashed line line).

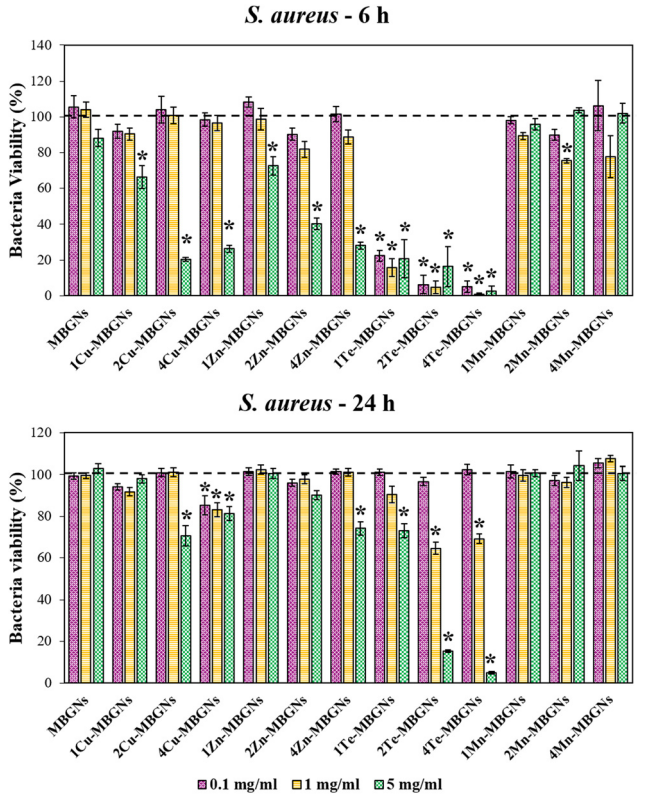

Fig. 7 *S. aureus* viabilities after 6 and 24 h treatment with the extracts of investigated MBGNs (samples in triplicates; mean values and SD from 4–6 measurements). The statistical significances ($p < 0.05$, marked by (*)) are depicted in comparison to the control (shown by dashed line).

co-culture assay.[39] Even though the antibacterial efficacy of Te has not been fully investigated, the effect is ascribed to TeO_3^{2-}, which is produced as a result of Te-MBGNs degradation.[40] It is reported that ROS generation is triggered by TeO_2^{3-} which can lead to oxidative stress as a result of superoxide radicals formation.[37,55] The activity of superoxide dismutase is found to be affected by TeO_3^{2-}, leading to the incapability to eradicate the ROS produced by Fenton's reaction, thereby accumulating in the cytoplasm and leading to toxicity.[40,56] The obtained results also revealed that with the higher extract concentration of 5 mg ml^{-1}, the reduction of *E. coli* and *S. aureus* viabilities was higher for Cu-MBGNs and Zn-MBGNs as compared to extracts from Mn-MBGNs, thereby confirming the role of Cu and Zn in the observed antibacterial efficacy. Our ion release findings showed that with increasing contents of Cu and Zn in the MBGNs composition, higher amounts of Cu (around 8–17 mg l^{-1}) and Zn (around 2–11 mg l^{-1}) were released in LB medium after 24 incubations, which can play an important role in the antibacterials activity of these compositions. These results suggested that Cu-MBGNs and Zn-MBGNs could reduce the bacteria viabilities in ion concentration and dose-dependent manners. As the previous studies suggested, the mechanism of action behind the antibacterial effect of Zn is correlated to its interaction with the bacterial membrane which changes the membrane permeability, leading to cytoplasm leakage and cell death.[57,58] The antibacterial effect of Cu is also ascribed to the hydroxyl radicals production which participate in some detrimental reactions such as proteins and lipids oxidation, resulting in bacteria damage.[59]

3.4. Cell viability assay

Depending on the concentrations, extracts or leachable products, biomaterials applied on an injured area can stimulate cytotoxicity against cells and may result in changing the morphology, adhesion or proliferation of cells. Therefore, biocompatibility is one of the vital requirements of biomaterials utilized for biomedical applications which needs to be assessed firstly *in vitro* and then *in vivo*.[60,61] In this study, to assess the biocompatibility, the WST-8 assay was performed after 48 h incubation of NHDF cells with extracts of the nanoparticles. Fig. 8(a) shows an schematic diagram of the WST-8 assay and results are presented in Fig. 8(b)–(f). Except for 4Te-MBGNs (Fig. 8(e)) which significantly led to the lowest cell viability (~60%) at concentration of 1 mg ml^{-1} and did not meet the international standard for cytocompatibility (≥70% of cell viability to be considered as cytocompatible material),[61] the NHDF cell viabilities were higher than 80% when the cells were incubated with extracts of all other MBGNs at concentrations of 1 mg ml^{-1} and 0.1 mg ml^{-1} for 48 h, suggesting the

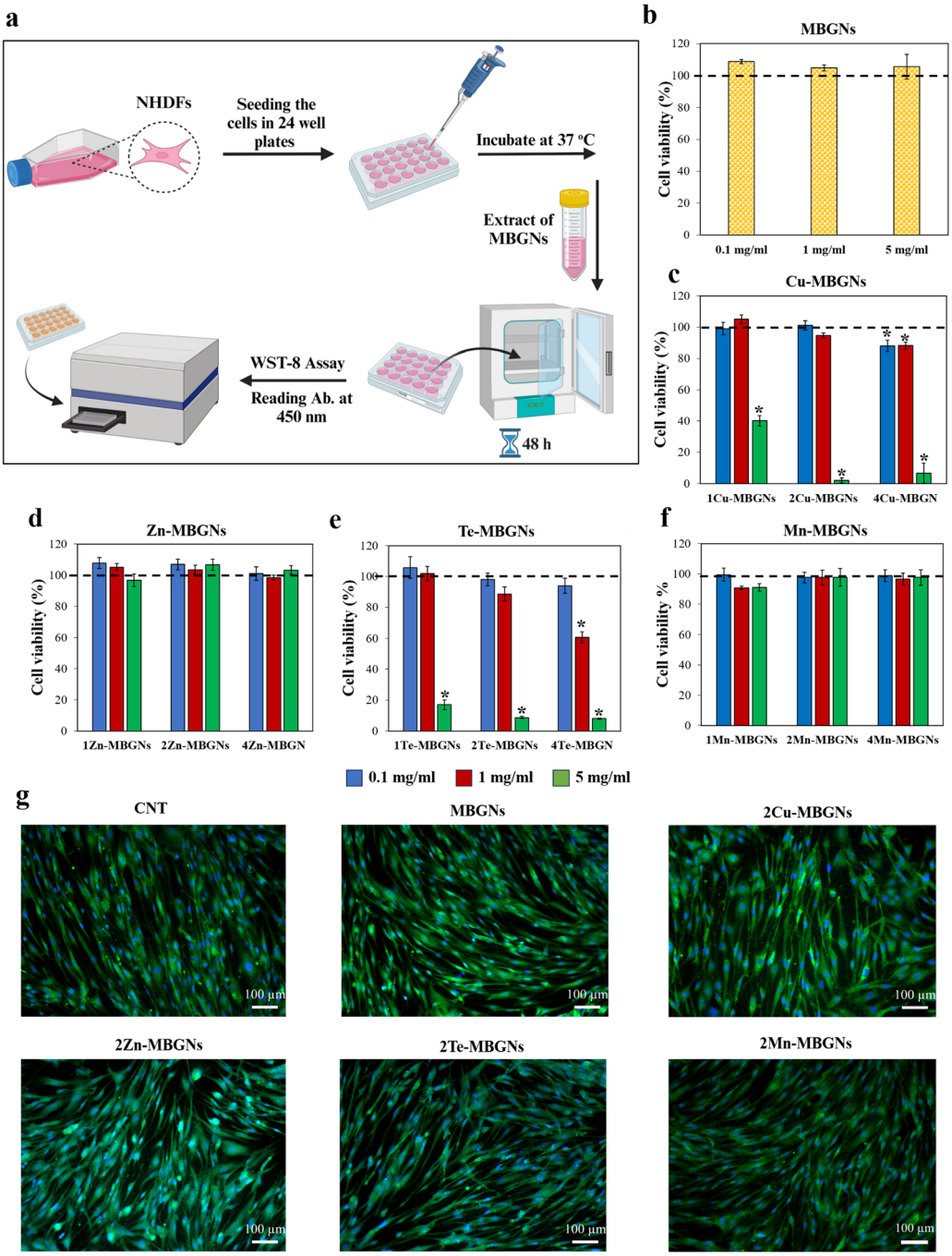

Fig. 8 (a) Schematic diagram demonstrating the WST-8 assay (created with biorender.com). (b)–(f) Viability of NHDF cells cultured with different concentration of the extracts (0.1, 1 and 5 mg ml^{-1}) for 48 h (samples in triplicates; mean values and SD from 6–9 measurements). The statistical significance (*; $p < 0.05$) was indicated as compared to CNT (dashed line). (g) Fluorescence microscopy images of Calcein (green) and DAPI (blue)-stained NHDF cells cultured with the extracts of 1 mg ml^{-1} nanoparticles.

nanoparticles' cytocompatibility. Based on the results of ion release studies in DMEM (Fig. 4), Cu (around 9–15 mg l^{-1}) and Te (around 11–30 mg l^{-1}) were released at higher concentrations as compared to Zn (around 2–6 mg l^{-1}) and Mn (around 1.7–3.6 mg l^{-1}) after 1 day incubation in DMEM. According to these results, it can be assumed that the root cause of the reduced viability of NHDF cells in the presence of 2–4Cu-MBGNs and 2–4Te-MBGNs extracts is related to the release of Cu and Te ions from the nanoparticles at concentrations of 15 mg l^{-1} and 22–30 mg l^{-1}, respectively.

Moreover, at high concentration (5 mg ml^{-1}), while the NHDF cells cultured with extracts of MBGNs, Zn-MBGNs and Mn-MBGNs demonstrated higher cell viabilities (>80%), the extracts of Cu-MBGNs and Te-MBGNs containing 1–4 mol% of Cu and Te showed cytotoxicity and the viability of NHDF cells was significantly reduced (~40% or less) as compared to the

control. This behavior could be attributed to the released Cu and Te ions in relatively high concentrations.

There are few studies that have evaluated the cytotoxicity effect of Te and Cu-containing bioactive glasses. Miola *et al.*, showed that Te is not toxic towards human bone marrow-derived stem cells (hBMSCs) when it was incorporated into bioactive glasses in a concentration of 5 mol%.[39] However, in another study by Zhang *et al.*, it was demonstrated that MBGNs containing 3 and 5 mol% Te inhibited MG63 cell viability in concentrations >40 μg ml^{-1}. From our results, it can be concluded that the nanoparticle dosages and concentrations of Te and Cu could affect the cytotoxicity of Te-MBGNs and Cu-MBGNs towards NHDF cells.

In addition to the WST-8 assay, calcein/DAPI staining was performed to visualize the morphology of cells cultured with 1 mg ml^{-1} extracts of the MBGNs, 2Cu-MBGNs, 2Zn-MBGNs, 2Te-MBGNs and 2Mn-MBGNs, which showed cytocompatibility with $>80\%$ cell viability. As depicted in Fig. 8(g), the cytoplasm and nuclei of viable NHDF cells appeared green and blue under fluorescence microscopy, respectively. The cells were well adhered to the wells showing typical morphology of NHDF cells just as the cells in the control group treated with DMEM (CNT) and no sign of morphological changes was observed, demonstrating that the dissolution products of the nanoparticles were cytocompatible towards NHDF cells (Fig. 8(g)).

3.5. Hemolysis evaluation

Hemocompatibility is one of the vital requirements for the biomaterials intended to be utilized in the biomedical field, particularly biomaterials used for hemostatic and wound healing applications and according to the international standards, the hemolysis rate induced by a material should be less than 5% to be considered as a hemocompatible material.[62] Hemolysis is known by breakdown or destruction of RBCs membranes which results in hemoglobin leakage from RBCs into the plasma (Fig. 9(a)).[63] Therefore, in this study to assess the blood compatibility of undoped and doped MBGNs, the hemoglobin release was evaluated in the supernatant of the RBCs treated with the MBGNs *via* measuring the absorbance of supernatants. The results of the hemolysis assay are shown in Fig. 9(b). All the MBGNs in the concentration of 1 mg ml^{-1} exhibited hemolysis ratios lower than 1% Triton X-100 as positive control, which disturbed the membrane of the RBCs. However, donor-dependent differences were observed for the nanoparticles and some donors were more sensitive as compared to others. For instance, in donor 1, except Te-MBGNs which demonstrated significantly higher hemolysis ratio than negative control (PBS) and were found to have the most potent hemolytic effect (hemolysis ratio above the international standard of 5%), the rest of nanoparticles were found to be hemocompatible as they presented $<5\%$ of hemolysis. Notably, the hemolytic effect of the Te-MBGNs was found to be enhanced with increasing the amount of Te. Some studies have reported that Te compounds can provoke hemolysis in human RBCs *in vitro*.[64,65] For instance, tellurite was reported to damage membranes resulting in glutathione (GSH) depletion, leading to hemolysis.[66,67] However, good blood compatibility of Te nanowires (TeNWs) was reported in another study by Wu *et al.*, so that at a concentration of 50 μg ml^{-1}, no rupture of RBCs was observed by TeNWs.[68] In donor 2, while 4Cu-MBGN, 2Zn-MBGN, 2 and 4Mn-MBGNs were found to be hemocompatible, the rest of the nanoparticles showed hemolysis of $>5\%$.

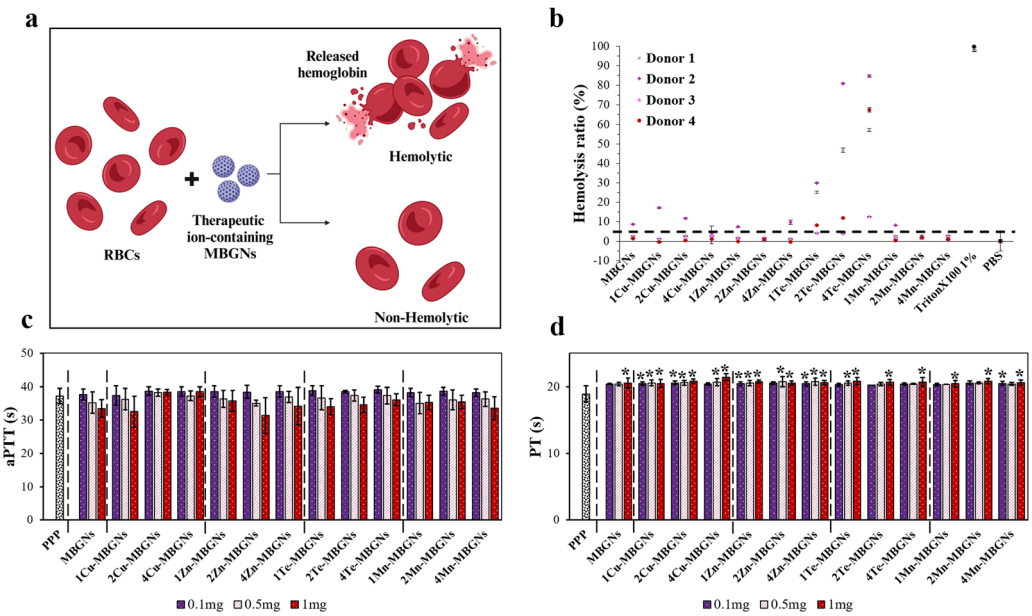

Fig. 9 (a) Schematic illustration of effect of therapeutic ions-containing MBGNs on RBCs, leading to hemolysis or no hemolysis (created with Biorender.com); (b) hemolysis ratios of MBGNs containing different concentrations of Cu, Zn, Te and Mn. The dashed line indicates the level of safe hemolysis ratio based on the international standard; effect of the nanoparticles on (c) aPTT and (d) PT values. The statistical significance ($p < 0.05$) marked by (*) are demonstrated as compared to PPP.

Furthermore, in donor 3, except 4Te-MBGN which led to the hemolysis greater than 5%, all the MBGNs, Cu-MBGNs, Zn-MBGNs, Mn-MBGNs and 1–2 Te-MBGNs were found to be hemocompatible. Interestingly, donor 4 demonstrated the same tendency of donor 1 and except Te-MBGNs which was found to be hemolytic, the rest of the nanoparticles resulted in lower hemolysis ($<5\%$), indicating their good hemocompatibility.

3.6. Effect of nanoparticles on the early stage of wound healing

Hemostasis is the first reaction that immediately initiates when a wound appears, leading to blood clot formation and thus stoppage of bleeding. Even though this stage is short, designing and engineering biomaterials with capability to accelerate hemostasis is favorable for wound treatment.[35] Therefore, in this study to assess the effect of MBGNs on hemostasis as the early stage of wound healing, both aPTT and PT which measure times taken to activate intrinsic and extrinsic pathways of the coagulation cascade, respectively, were investigated. For consistency between the results of antibacterial studies, biocompatibility, hemolysis and blood coagulation studies, three different concentrations, namely; 10, 5, 1 mg of the nanoparticles, were incubated with PPP from healthy donors. The suspensions were further diluted to make the final concentrations of 0.1, 0.5 and 1 mg ml^{-1}. While the plasma treated with the MBGNs showed a slightly prolonged PT, some of the nanoparticles with different compositions shortened aPTT in an amount-dependent manner so that with increasing concentration of the nanoparticles from 0.1 to 1 mg ml^{-1}, aPTT was shortened (Fig. 9(c) and (d)). Among the various tested nanoparticles, MBGNs, 1Cu-MBGNs, 2Zn-MBGNs, 1Te-MBGNs, and 4Mn-MBGNs resulted in lower aPTT values at the concentration of 1 mg ml^{-1} as comparted to the rest of the compositions. Hemostatic activities of the porous bioactive glasses containing various therapeutic ions have been recognized in recent years.[11,14] One of the key factors affecting the clotting activity of bioactive glasses is the release of Ca ions, which are well established ions inducing the intrinsic pathway of the coagulation cascade, thereby enhancing thrombin production for rapid generation of fibrin and accelerating the blood coagulation.[11,17] In addition to the high surface area of porous bioactive glasses which results in high capacity of water absorption from blood and therefore concentration of the blood components, the presence of negatively charged silanol groups which can activate intrinsic pathways of the coagulation cascade *via* binding to the clotting factor XII (contact activation) is another crucial factor contributing to the clotting activity of bioactive glasses.[49,50] Besides the mentioned parameters affecting the hemostatic function of bioactive glasses, the presence of some other therapeutic ions can further enhance their hemostatic activities.[11,14] For instance, the release of Zn ions from platelets at the injured sites as well as from external sources could stimulate the activation of the coagulation factor XII, boosting platelet aggregation and fibrin clot formation.[35,69–71] In a study by Pan *et al.*, microspheres composed of chitosan and Zn–alginate were fabricated and the results revealed that the released Zn ions from the microspheres contributed to the hemostatic activity *via* activation of coagulation factor XII.[69]

Taken into account the aforementioned explanation and the findings of this study, it could be concluded that the nanoparticles assessed herein have potential to influence aPTT values and therefore the intrinsic pathway of the coagulation cascade, depending on the concentrations of therapeutic ions as well as the concentration of applied nanoparticles. However, in spite of decreasing aPTT values with utilization of 1 mg ml^{-1} of MBGNs, 1Cu-MBGNs, 2Zn-MBGNs, 1Te-MBGNs, and 4Mn-MBGNs, there are no significant differences between these compositions as well as with respect to PPP. Of particular importance, as very low concentrations of the nanoparticles (0.1–1 mg ml^{-1}) were utilized in this study, further investigations may need to be carried out to deepen our understanding of the effect of therapeutic ions and dose of applied nanoparticles on the activation of the coagulation cascade in higher concentrations while preserving biocompatibility and hemocompatibility.

3.7. Wound scratch assay

It is acknowledged that fibroblast cells have a crucial contribution in all inflammatory, proliferation and remodeling phases of wound healing.[72] Notably, the recruitment of immune cells can be modulated by fibroblasts during the inflammatory phase. The cells are also found to regulate the behavior and survival of the immune cells in damaged tissue. During the proliferation phase, fibroblast cells migrate into the injured site, proliferate and promote angiogenesis and granulation tissue formation *via* secreting pro-angiogenic factors. During this phase, fibroblasts also differentiate into myofibroblasts which play a key role in the remodeling phase of wound healing.[72] Therefore, in this study, the impact of the dissolution products of MBGNs, Cu-MBGNs, Zn-MBGNs, Te-MBGNs and Mn-MBGNs on migration of NHDF cells was investigated *in vitro via* the scratch assay. The assay is schematically indicated in Fig. 10(a). As can be seen in Fig. 10(b), with increasing concentrations of Cu, Zn, Te and Mn, migration of NHDF cells in scratch areas appeared to occur significantly slower than in the CNT group and wound closure rates were higher for MBGNs (86 ± 4), 1 and 2Zn-MBGNs (76 ± 2 and 78 ± 5, respectively), 1Te-MBGNs (79 ± 5) and 1Mn-MBGNs (76 ± 6) with respect to those of the other nanoparticles and no significant differences were observed in comparison to the CNT group (91 ± 2). Similar to the results of cell viability assay, where the extracts of MBGNs with higher concentrations of Cu and Te reduced NHDF cell viability, the migration of the NHDF cells in the scratch areas was more inhibited when the cells were treated with these extracts. Nevertheless, as can be seen from Fig. 10(c), the scratch widths at 24 h treatment were reduced in comparison to 0 h, suggesting that the NHDF cells can migrate under treatment with the extracts of doped and undoped MBGNs but at a slower rate than for the untreated group (CNT).

In recent years, bioactive glasses incorporating therapeutic ions have shown promise for wound healing applications.[12,13,73] The ionic products of bioactive glasses released in the wound area

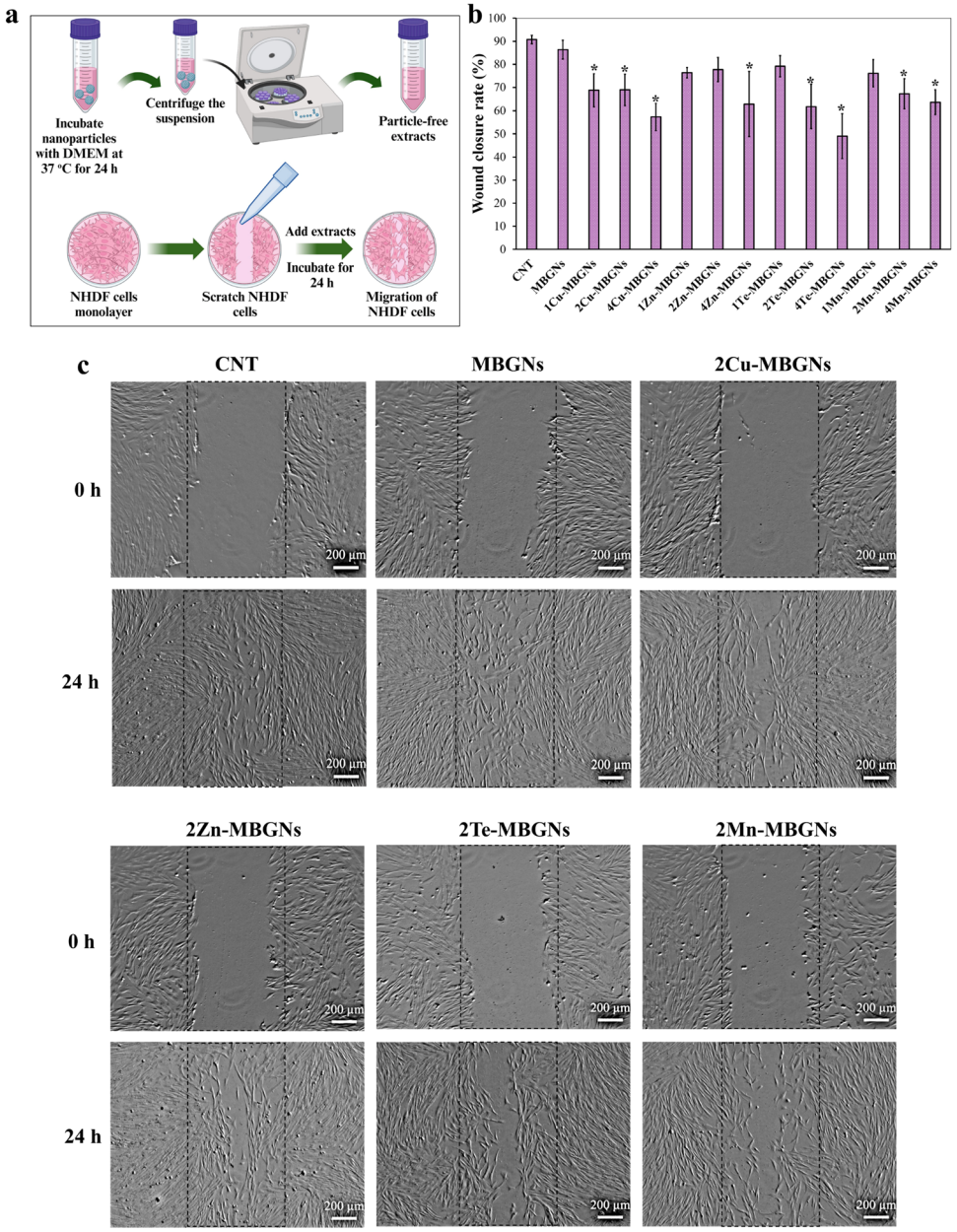

Fig. 10 (a) Schematic diagram illustrating the *in vitro* scratch assay (created with biorender.com). (b) *In vitro* wound closure rates after 24 h treatment of scratch areas with the extract of MBGNs at the concentration of 1 mg ml^{-1} (samples in triplicates; mean values and SD from 3 measurements). (c) Representative images of scratches created on NHDF cell monolayers and the wound closure after 24 h treatment.

have been shown to stimulate the different stages of the wound healing process.[13] It is also reported that upon immersion of bioactive glasses in biological environments, hydroxyapatite formation can be induced, which may affect the wound healing process. In an early study by Ostomel *et al.*, pure hydroxyapatite was found to have anti-thrombotic effect as it led to a decrease in clot strength and blood coagulation rate.[74] They also reported that spherical bioactive glasses in the system of SiO_2–CaO–P_2O_5 with low Si/Ca ratio and rapid hydroxyapatite deposition rate can lead to slower and less blood coagulation rate.[75] On the other hand, some studies showed that hydroxyapatite-containing biomaterials may result in the acceleration of the wound healing process.[76,77] Chen *et al.* reported that borate bioactive glass coated with hydroxyapatite (nano-HCA@BG) resulted in higher 3T3-L1 cell migration as compared to the borate bioactive glass (BBG) without coating. *In vivo* results in rodent models also revealed that nano-HCA@BG led to the highest wound healing rate of 98 ± 2% in comparison to 68 ± 4% and 61 ± 2.6% for the wound treated with BBG and nano-HA, respectively.[76] However, the effect of hydroxyapatite formation on wound healing is yet to be determined and more investigations are needed to specify the correlation between the wound healing rate and possible hydroxyapatite formation on the surface of doped and undoped MBGNs. It is also reported that undesired soft tissue calcification may be a risk associated with the

apatite-forming capability of bioactive glasses.[78–81] On the other hand, when acute and chronic wounds with neutral to alkaline pH are successfully healed, hydroxyapatite crystals formed on bioactive glasses surfaces may be dissolved under the acidic pH (4.0–6.0) of healed skin.[13] Nevertheless, bioactive glasses should preferably resorb quicker than the occurrence of soft tissue calcification.[78,79] Even though silicate, borate or phosphate bioactive glasses are reported to dissolve in a controlled manner (from hours to weeks), the long-lasting effects of the dissolution products in skin and soft tissues should be evaluated in dedicated *in vivo* models.

4. Conclusions

Engineering bioactive glasses containing therapeutic biologically active ions is becoming one of the areas of increasing research efforts in the field of wound healing biomaterials. In this study MBGNs containing various concentrations of Cu, Zn, Te and Mn with spherical morphologies were developed *via* a microemulsion-assisted sol–gel technique and their therapeutic potential to promote hemostasis and wound healing was investigated. The results demonstrated that all MBGNs except the 4Te-MBGNs, retain a high surface area and a high pore volume. Depending on the therapeutic ions incorporated into MBGNs, the extracts were found to decrease bacteria viability and the effect was more pronounced when the amount of applied nanoparticles was increased. Moreover, MBGNs were in general cytocompatible with NHDF cells. However, our results indicated that the release of Te and Cu ions at high concentrations can negatively affect the growth and viability of NHDF cells.

Our study additionally demonstrated that the hemolysis behaviour of the nanoparticles was donor-dependent. Coagulation time (aPTT) and wound scratch assay were also affected by the addition of MBGNs. At the concentration of 1 mg ml^{-1}, while aPTT values of MBGNs, 1Cu-MBGNs, 2Zn-MBGNs, 1Te-MBGNs, and 4Mn-MBGNs were reduced in comparison to other nanoparticles, the rate of NHDF cell migration in the scratch area was higher for MBGNs, 1 and 2Zn-MBGNs, 1Te-MBGNs and 1Mn-MBGNs.

However, to further elucidate the effect of different therapeutic elements on hemostasis and wound healing, more *in vitro* and *in vivo* studies are required. One of the parameters that need to be evaluated is the essential concentration of applied MBGNs required to achieve their target biological functions to accelerate hemostasis and promote wound healing while maintaining their blood compatibilities and cytocompatibilities. In addition, the characterisation of the oxidation states of the doped elements, not investigated in this work, should be considered in future studies, *e.g.* by XPS surface analysis, as this property will likely have an effect on the biological activity of the ions. Moreover, synergistic effects of simultaneous release of Cu, Zn, Te and Mn remain the topic of future studies.

Data availability

The data are available from the corresponding authors upon reasonable request.

Conflicts of interest

There are no conflicts of interest to declare.

Acknowledgements

This work was supported by the Alexander von Humboldt Foundation. CJ is funded *via* the Professorship for AI-Guided Nanomaterials within the framework of the Hightech Agenda (HTA) of the Free State of Bavaria. The ICP study was supported by FunGlass (European Union's Horizon 2020 research and innovation programme, grant agreement no. 739566). The authors thank also Hans Wormser, Herzogenaurach, Germany for financial support.

References

1 Y. Zheng, K. Shariati, M. Ghovvati, S. Vo, N. Origer, T. Imahori, N. Kaneko and N. Annabi, *Biomaterials*, 2023, **301**, 122240.
2 D. A. Hickman, C. L. Pawlowski, U. D. Sekhon, J. Marks and A. S. Gupta, *Adv. Mater.*, 2018, **30**, 1700859.
3 J. Zhu, G. Jiang, G. Song, T. Liu, C. Cao, Y. Yang, Y. Zhang and W. Hong, *ACS Appl. Bio Mater.*, 2019, **2**, 5042–5052.
4 A. A. Rondas, J. M. Schols, E. E. Stobberingh and R. J. Halfens, *Int. Wound J.*, 2015, **12**, 630–635.
5 B. A. Mast and G. S. Schultz, *Wound Repair Regen.*, 1996, **4**, 411–420.
6 Y. Wang, T. Li, C. Xie, S. Li and B. Lei, *Bioact. Mater.*, 2023, **25**, 319–332.
7 B. Guo, R. Dong, Y. Liang and M. Li, *Nat. Rev. Chem.*, 2021, **5**, 773–791.
8 X. Wang, F. Cheng, J. Liu, J.-H. Smått, D. Gepperth, M. Lastusaari, C. Xu and L. Hupa, *Acta Biomater.*, 2016, **46**, 286–298.
9 G. Lokhande, J. K. Carrow, T. Thakur, J. R. Xavier, M. Parani, K. J. Bayless and A. K. Gaharwar, *Acta Biomater.*, 2018, **70**, 35–47.
10 J. Liu, X. Zhou, Y. Zhang, W. Zhu, A. Wang, M. Xu and S. Zhuang, *Mater. Today Chem.*, 2022, **23**, 100735.
11 S. Pourshahrestani, N. A. Kadri, E. Zeimaran and M. R. Towler, *Biomater. Sci.*, 2019, **7**, 31–50.
12 S. Naseri, W. C. Lepry and S. N. Nazhat, *J. Mater. Chem. B*, 2017, **5**, 6167–6174.
13 T. Mehrabi, A. S. Mesgar and Z. Mohammadi, *ACS Biomater. Sci. Eng.*, 2020, **6**, 5399–5430.
14 Y. Zheng, J. Wu, Y. Zhu and C. Wu, *Chem. Sci.*, 2023, **14**, 29–53.
15 X. Yan, C. Yu, X. Zhou, J. Tang and D. Zhao, *Angew. Chem., Int. Ed.*, 2004, **43**, 5980–5984.
16 M. Vallet-Regi and A. J. Salinas, *Mater. Today Bio*, 2021, **11**, 100121.
17 C. Dai, Y. Yuan, C. Liu, J. Wei, H. Hong, X. Li and X. Pan, *Biomaterials*, 2009, **30**, 5364–5375.

18 S. Pourshahrestani, E. Zeimaran, N. A. Kadri, N. Gargiulo, S. Samuel, S. V. Naveen, T. Kamarul and M. R. Towler, *J. Mater. Chem. B*, 2016, **4**, 71–86.
19 M. Nagrath, R. Gallant, A. R. Yazdi, A. Mendonca, S. Rahman, L. Chiu, S. D. Waldman, H. Ni and M. R. Towler, *J. Biomater. Appl.*, 2021, **35**, 924–932.
20 J. Du, L. Fan, J. M. Razal, S. Chen, H. Zhang, H. Yang, H. Li and J. Li, *J. Mater. Chem. B*, 2023, **11**, 7364–7377.
21 Y. Zhang, J. Liu, Z. Wu, X. Mei, W. Zhu and A. Wang, *Mater. Today Chem.*, 2022, **25**, 100980.
22 T. E. Paterson, A. Bari, A. J. Bullock, R. Turner, G. Montalbano, S. Fiorilli, C. Vitale-Brovarone, S. MacNeil and J. Shepherd, *Front. Bioeng. Biotechnol.*, 2020, **8**, 246.
23 K. Zheng, F. Bider, M. Monavari, Z. Xu, C. Janko, C. Alexiou, A. M. Beltrán and A. R. Boccaccini, *Regener. Biomater.*, 2024, **11**, rbad105.
24 S. Kargozar, M. Mozafari, S. Hamzehlou and F. Baino, *Front. Bioeng. Biotechnol.*, 2019, **7**, 62.
25 J. Liu, X. Zhou, Y. Zhang, A. Wang, W. Zhu, M. Xu and S. Zhuang, *J. Biomed. Mater. Res., Part B*, 2022, **110**, 1255–1264.
26 L. B. Romero-Sánchez, M. Marí-Beffa, P. Carrillo, M. Á. Medina and A. Díaz-Cuenca, *Acta Biomater.*, 2018, **68**, 272–285.
27 F. Kermani, S. Nazarnezhad, Z. Mollaei, S. Mollazadeh, A. Ebrahimzadeh-Bideskan, V. R. Askari, R. K. Oskuee, A. Moradi, S. A. Hosseini and Z. Azari, *Int. J. Mol. Sci.*, 2023, **24**, 1304.
28 Y. Hou, Y. Xia, Y. Pan, S. Tang, X. Sun, Y. Xie, H. Guo and J. Wei, *Mater. Sci. Eng., C*, 2017, **76**, 340–349.
29 K. Zheng, Y. Fan, E. Torre, P. Balasubramanian, N. Taccardi, C. Cassinelli, M. Morra, G. Iviglia and A. R. Boccaccini, *Part. Part. Syst. Charact.*, 2020, **37**, 2000054.
30 P. Roy, R. Saha and J. Chakraborty, *Ceram. Int.*, 2023, **49**, 6389–6400.
31 S. Zhao, L. Li, H. Wang, Y. Zhang, X. Cheng, N. Zhou, M. N. Rahaman, Z. Liu, W. Huang and C. Zhang, *Biomaterials*, 2015, **53**, 379–391.
32 S. Kargozar, M. Mozafari, S. Ghodrat, E. Fiume and F. Baino, *Mater. Sci. Eng., C*, 2021, **121**, 111741.
33 A. Bari, N. Bloise, S. Fiorilli, G. Novajra, M. Vallet-Regí, G. Bruni, A. Torres-Pardo, J. M. González-Calbet, L. Visai and C. Vitale-Brovarone, *Acta Biomater.*, 2017, **55**, 493–504.
34 P.-H. Lin, M. Sermersheim, H. Li, P. H. Lee, S. M. Steinberg and J. Ma, *Nutrients*, 2017, **10**, 16.
35 H. Wang, Z. Xu, Q. Li and J. Wu, *Eng. Regen.*, 2021, **2**, 137–153.
36 U. Pantulap, M. Arango-Ospina and A. R. Boccaccini, *J. Mater. Sci.: Mater. Med.*, 2022, **33**, 1–41.
37 L. A. Ba, M. Döring, V. Jamier and C. Jacob, *Org. Biomol. Chem.*, 2010, **8**, 4203–4216.
38 E. O. Alvarez, O. J. Sacchi and S. G. Ratti, *J. Neurorestoratol.*, 2021, **9**, 151–163.
39 M. Miola, J. Massera, A. Cochis, A. Kumar, L. Rimondini and E. Vernè, *Mater. Sci. Eng., C*, 2021, **123**, 111957.
40 Y. Zhang, M. Hu, W. Zhang and X. Zhang, *J. Colloid Interface Sci.*, 2022, **610**, 719–730.
41 L. Huang, M. Liu, Z. Feng, X. Xu, L. Chen, Z. Ma and L. Li, *Mater. Today Bio*, 2022, **15**, 100271.
42 F. Westhauser, S. Wilkesmann, Q. Nawaz, S. I. Schmitz, A. Moghaddam and A. R. Boccaccini, *J. Biomed. Mater. Res., Part A*, 2020, **108**, 1806–1815.
43 Z. Wu, H. Zhuang, B. Ma, Y. Xiao, B. Koc, Y. Zhu and C. Wu, *Research*, 2021, **2021**, 9780943.
44 Q. Liang, Q. Hu, G. Miao, B. Yuan and X. Chen, *Mater. Lett.*, 2015, **148**, 45–49.
45 K. Zheng, J. Kang, B. Rutkowski, M. Gaweda, J. Zhang, Y. Wang, N. Founier, M. Sitarz, N. Taccardi and A. R. Boccaccini, *Front. Chem.*, 2019, **7**, 497.
46 Z. Neščáková, K. Zheng, L. Liverani, Q. Nawaz, D. Galusková, H. Kaňková, M. Michálek, D. Galusek and A. R. Boccaccini, *Bioact. Mater.*, 2019, **4**, 312–321.
47 Q. Nawaz, M. A. U. Rehman, A. Burkovski, J. Schmidt, A. M. Beltrán, A. Shahid, N. K. Alber, W. Peukert and A. R. Boccaccini, *J. Mater. Sci.: Mater. Med.*, 2018, **29**, 1–13.
48 S. Pourshahrestani, N. A. Kadri, E. Zeimaran, N. Gargiulo, S. Samuel, S. V. Naveen, K. Hasikin, T. Kamarul and M. R. Towler, *Biomed. Mater.*, 2018, **13**, 025020.
49 X. Sun, Z. Tang, M. Pan, Z. Wang, H. Yang and H. Liu, *Carbohydr. Polym.*, 2017, **177**, 135–143.
50 C. Wang, H. Zhou, H. Niu, X. Ma, Y. Yuan, H. Hong and C. Liu, *Biomater. Sci.*, 2018, **6**, 3318–3331.
51 G. Carotenuto, M. Palomba, S. De Nicola, G. Ambrosone and U. Coscia, *Nanoscale Res. Lett.*, 2015, **10**, 1–8.
52 A. K. Solanki, H. Autefage, A. R. Rodriguez, S. Agarwal, J. Penide, M. Mahat, T. Whittaker, A. Nommeots-Nomm, E. Littmann and D. J. Payne, *Front. Bioeng. Biotechnol.*, 2023, **11**, 1125060.
53 U. Pantulap, I. Unalan, K. Zheng and A. R. Boccaccini, *J. Porous Mater.*, 2024, **31**, 685–696.
54 A. Hoppe, N. S. Güldal and A. R. Boccaccini, *Biomaterials*, 2011, **32**, 2757–2774.
55 D. M. Cruz, W. Tien-Street, B. Zhang, X. Huang, A. V. Crua, A. Nieto-Argüello, J. L. Cholula-Díaz, L. Martínez, Y. Huttel and M. U. González, *Green Chem.*, 2019, **21**, 1982–1998.
56 R. J. Turner, R. Borghese and D. Zannoni, *Biotechnol. Adv.*, 2012, **30**, 954–963.
57 N. Mutlu, L. Liverani, F. Kurtuldu, D. Galusek and A. R. Boccaccini, *Int. J. Biol. Macromol.*, 2022, **213**, 845–857.
58 M. Godoy-Gallardo, U. Eckhard, L. M. Delgado, Y. J. de Roo Puente, M. Hoyos-Nogués, F. J. Gil and R. A. Perez, *Bioact. Mater.*, 2021, **6**, 4470–4490.
59 C. Wu, Y. Zhou, M. Xu, P. Han, L. Chen, J. Chang and Y. Xiao, *Biomaterials*, 2013, **34**, 422–433.
60 C. Ghobril and M. Grinstaff, *Chem. Soc. Rev.*, 2015, **44**, 1820–1835.
61 S. Guo, M. Yao, D. Zhang, Y. He, R. Chang, Y. Ren and F. Guan, *Adv. Healthcare Mater.*, 2022, **11**, 2101808.
62 S. Liu, N. Jiang, Y. Chi, Q. Peng, G. Dai, L. Qian, K. Xu, W. Zhong and W. Yue, *ACS Biomater. Sci. Eng.*, 2022, **8**, 3754–3764.

63 M. Nikfar, M. Razizadeh, J. Zhang, R. Paul, Z. J. Wu and Y. Liu, *Artif. Organs*, 2020, **44**, E348–E368.
64 V. P. P. Schiar, D. B. Dos Santos, M. W. Paixão, C. W. Nogueira, J. B. T. Rocha and G. Zeni, *Chem.-Biol. Interact.*, 2009, **177**, 28–33.
65 V. P. P. Schiar, D. B. Dos Santos, D. S. Lüdtke, F. Vargas, M. W. Paixão, C. W. Nogueira, G. Zeni and J. B. T. Rocha, *Toxicol. In Vitro*, 2007, **21**, 139–145.
66 R. De Meio and D. O'Leary, *J. Am. Osteopath. Assoc.*, 1975, **75**, 430–431.
67 E. Domínguez-Álvarez, B. Rácz, M. A. Marć, M. J. Nasim, N. Szemerédi, J. Viktorová, C. Jacob and G. Spengler, *Drug Resist. Updates*, 2022, **63**, 100844.
68 Y. Wu, T. Guo, Y. Qiu, Y. Lin, Y. Yao, W. Lian, L. Lin, J. Song and H. Yang, *Chem. Sci.*, 2019, **10**, 7068–7075.
69 M. Pan, Z. Tang, J. Tu, Z. Wang, Q. Chen, R. Xiao and H. Liu, *Mater. Sci. Eng., C*, 2018, **85**, 27–36.
70 T. T. Vu, J. C. Fredenburgh and J. I. Weitz, *Thromb. Haemostasis*, 2013, **109**, 421–430.
71 I. Schousboe, *Blood Coagulation Fibrinolysis*, 1993, **4**, 671–678.
72 F. Cialdai, C. Risaliti and M. Monici, *Front. Bioeng. Biotechnol.*, 2022, **10**, 958381.
73 V. Miguez-Pacheco, L. L. Hench and A. R. Boccaccini, *Acta Biomater.*, 2015, **13**, 1–15.
74 T. A. Ostomel, Q. Shi and G. D. Stucky, *J. Am. Chem. Soc.*, 2006, **128**, 8384–8385.
75 T. A. Ostomel, Q. Shi, C. K. Tsung, H. Liang and G. D. Stucky, *Small*, 2006, **2**, 1261–1265.
76 R. Chen, Q. Li, S. Xu, J. Han, P. Huang, Z. Yu, D. Jia, J. Liu, H. Jia and M. Shen, *Chem. Eng. J.*, 2021, **426**, 130299.
77 H. Donya, R. Darwesh and M. Ahmed, *Int. J. Biol. Macromol.*, 2021, **186**, 897–908.
78 S. Kargozar, S. Hamzehlou and F. Baino, *Mater. Sci. Eng., C*, 2019, **97**, 1009–1020.
79 S. Kargozar, R. K. Singh, H.-W. Kim and F. Baino, *Acta Biomater.*, 2020, **115**, 1–28.
80 R. Sergi, V. Cannillo, A. R. Boccaccini and L. Liverani, *Materials*, 2020, **13**, 5651.
81 K. Schuhladen, P. Mukoo, L. Liverani, Z. Neščáková and A. R. Boccaccini, *Biomed. Mater.*, 2020, **15**, 065002.